

Nonlinear coherent light-matter interaction in 2D MoSe₂ nanoflakes for all-optical switching and logic applications

Sk Kalimuddin[†], Biswajit Das[†], Nabamita Chakraborty, Madhupriya Samanta, Satyabrata Bera, Arnab Bera, Deep Singha Roy, Suman Kalyan Pradhan, Kalyan K. Chattopadhyay* and Mintu Mondal*

Sk Kalimuddin, Dr. B. Das, S. Bera, A. Bera, D. S. Roy, Dr. S. K. Pradhan, Dr. M. Mondal
School of Physical Sciences, Indian Association for the Cultivation of Science, Jadavpur, Kolkata 700032, India

Email Address: Mintu.Mondal@iacs.res.in

M. Samanta

Department of Electronics & Telecommunication Engineering, Jadavpur University, Kolkata-700032, India

N. Chakraborty, Prof. K. K. Chattopadhyay

Thin film & Nanoscience lab, Department of Physics, Jadavpur University, Kolkata-700032, India

Email Address: kalyan_chatopadhyay@yahoo.com

[†] These authors contributed equally to this work

Keywords: *MoSe₂, Kerr nonlinearity, Spatial self-phase modulation, all-optical modulation, all-optical logic gates*

We report a strong nonlinear optical response of 2D MoSe₂ nanoflakes (NFs) through spatial self-phase modulation (SSPM) and cross-phase modulation (XPM) induced by nonlocal coherent light-matter interactions. The coherent interaction of light and MoSe₂ NFs creates the SSPM of laser beams, forming concentric diffraction rings. The nonlinear refractive index (n_2) and the third-order broadband nonlinear optical susceptibility ($\chi^{(3)}$) of MoSe₂ NFs are determined from the self diffraction pattern at different exciting wavelengths of 405, 532, and 671 nm with varying the laser intensity. The evolution and deformation of diffraction ring patterns are observed and analyzed by the ‘wind-chime’ model and thermal effect. By taking advantage of the reverse saturated absorption of 2D SnS₂ NFs compared to MoSe₂, an all-optical diode has been designed with MoSe₂/SnS₂ hybrid structure to demonstrate the non-reciprocal light propagation. Also a few other optical devices based on MoSe₂ and other semiconducting materials such as Bi₂Se₃, CuPc, and graphene have been investigated. The all-optical logic gates and all-optical information conversion have been demonstrated through the XPM technique using two laser beams. The proposed optical scheme based on MoSe₂ NFs has been demonstrated as a potential candidate for all-optical nonlinear photonic devices such as all-optical diodes and all-optical switches.

1 Introduction

Optical responses of two-dimensional (2D) nanomaterials have drawn much attention due to their strong nonlinear characteristics and broadband Kerr nonlinearity for their potential applications in photonic devices. The strong light-matter interactions in two-dimensional (2D) materials produce many interesting nonlinear optical phenomena, and quasiparticle excitations that can have far-reaching implications in science and technology [1, 2, 3]. Therefore, 2D nanomaterials have attracted significant attention from fundamental physics to applied sciences as a scientific platform for studying nonlinear optical phenomena and optoelectronic devices [4, 5]. The nonlinear optical response has been investigated using the following three main methods that are four-wave mixing, Z-scan, and spatial self-phase modulation (SSPM) spectroscopy [6, 7, 8]. The four-wave mixing and Z-scan spectroscopy require a complicated experimental setup, while similar results can be obtained in the SSPM with a simple, straightforward technique. Therefore, SSPM spectroscopy has become an effective tool for studying the nonlinear optical properties of the materials like nonlinear refractive index (n_2), and third-order nonlinear susceptibility ($\chi^{(3)}$) [9, 10, 11]. In this experiment, strong coherent light-matter interaction creates spatial phase modulation of the incident laser light and produces diffraction ring patterns in the far field. Durbin et al. first observed the SSPM in liquid crystals, and recently, in 2011, Wu et al. investigated the third-order nonlinear susceptibility in exfoliated graphene by the SSPM method [12, 13, 14]. After that, there has been a significant increase in interest in SSPM, and many groups have studied the nonlinear response of different types of materials.

The nonlinear interaction of light and materials leads to self diffraction rings/patterns in the far-field due to the SSPM. The formation, expansion, and collapse process of the diffraction rings with time has

been described by the ‘wind-chime’ model based on the nonlocal electric coherent theory [15]. In this model, the samples are being polarized because of interaction between the samples (layered nanostructures) and incident coherent light beam [16, 17]. Based on the energy relaxation process, the samples are reoriented from an arbitrary angle to the direction of the electric field of the incident light beam [18]. Although the above model describes the SSPM phenomena quite well, there are still a few open questions, like how the relaxation process occurs with incident light energy, how the relaxation time depends upon the solvent viscosity, and the role of polar and non-polar solvents? Therefore a detailed study of SSPM with different materials and solvents is desired for in-depth understanding.

Recently, a significant amount of work has been done on various 2D materials, such as graphene, topological insulators, perovskite, transition metal dichalcogenides (TMDs), MXenes, black phosphorus, etc. [19, 20, 21, 22, 23], and different hybrid structures are also studied for photonic device application based on the SSPM method [24, 25, 26]. The transition metal dichalcogenides (TMDs) are attractive candidates due to their unique tunable bandstructure and superior optic-electronic properties. TMDs are composed of transition metal elements intercalated between chalcogen elements in layered structures[27]. In these materials, the adjacent layers are held together by the weak van der Waals forces [22]. One of the most prevalent members of TMD’s family is MoSe₂ which can be easily synthesized using various methods, including hydrothermal, sonochemical, chemical vapor deposition, etc. [28, 29, 30, 31]. The MoSe₂ are being widely explored for multiple potential applications, such as water splitting, catalysts, batteries, photoelectrochemical, solar cells, sensors, etc. [32, 33, 34, 35, 36, 37]. However, the applications of MoSe₂ in photonics are still in their infancy [38].

So far, the SSPM method has been used to determine the third-order nonlinear susceptibility and the nonlinear refractive index of various semiconducting materials, but comparatively few optical devices are made for practical applications [27, 39]. Very few groups have devoted their attention to making novel optical logic gates using the SSPM technique for photonic devices [24, 40, 41]. These all-optical logic gates can open the paths toward many other all-optical signal processing such as optical networking, optical switching, optical computing, optical transmission, etc.[19]. Recently, all-optical switching and information converters based on SSPM have been demonstrated [40]. However, there are no reports/works on photonic devices based on MoSe₂ for all-optical logic applications.

In this work, we have experimentally investigated the nonlinear optical (NLO) properties of 2D MoSe₂ NFs using SSPM spectroscopy and designed a novel photonic diode. Furthermore, we have also presented a hybrid structure-based optical device for the realization of the ‘OR’ function for all-optical logic gates. We believe that this study will enhance the understanding of the nonlinear optical process in 2D materials and can lead to the development of optical devices based on the self-diffraction of light.

2 Results and discussion

2.1 Nonlinear Kerr effect : Nonlinear refractive index of MoSe₂ nanoflakes

The preparation of MoSe₂ NFs and its characterization are discussed in the experimental section 4 and presented in Figure 1. The Kerr nonlinear effect plays an important role in the study of the nonlinear optical response of 2D semiconducting (MoSe₂) materials. According to the nonlinear Kerr effect, the nonlinear refractive index can be expressed as $n = n_0 + n_2 I$, where I is the incident light intensity, n_0 and n_2 are the linear and nonlinear refractive index coefficient of the material, respectively [42]. The MoSe₂ is expected to have a strong Kerr nonlinear response. Therefore, the phase has a nonlinear modulating behavior to the transverse intensity profile of the incident Gaussian laser beam, and this nonlinear phase shift($\Delta\psi(r)$) can be expressed by [21],

$$\Delta\psi(r) = \frac{2\pi n_0}{\lambda} \int_0^{L_{eff}} n_2 I(r, z) dz \quad (1)$$

where λ is the wavelength of the laser, $r \in [0, +\infty)$ is the laser radial position, L_{eff} is the effective transmission length of the laser passing through the cuvette. This ‘self’ phase shift ($\Delta\psi$) gets modulated due

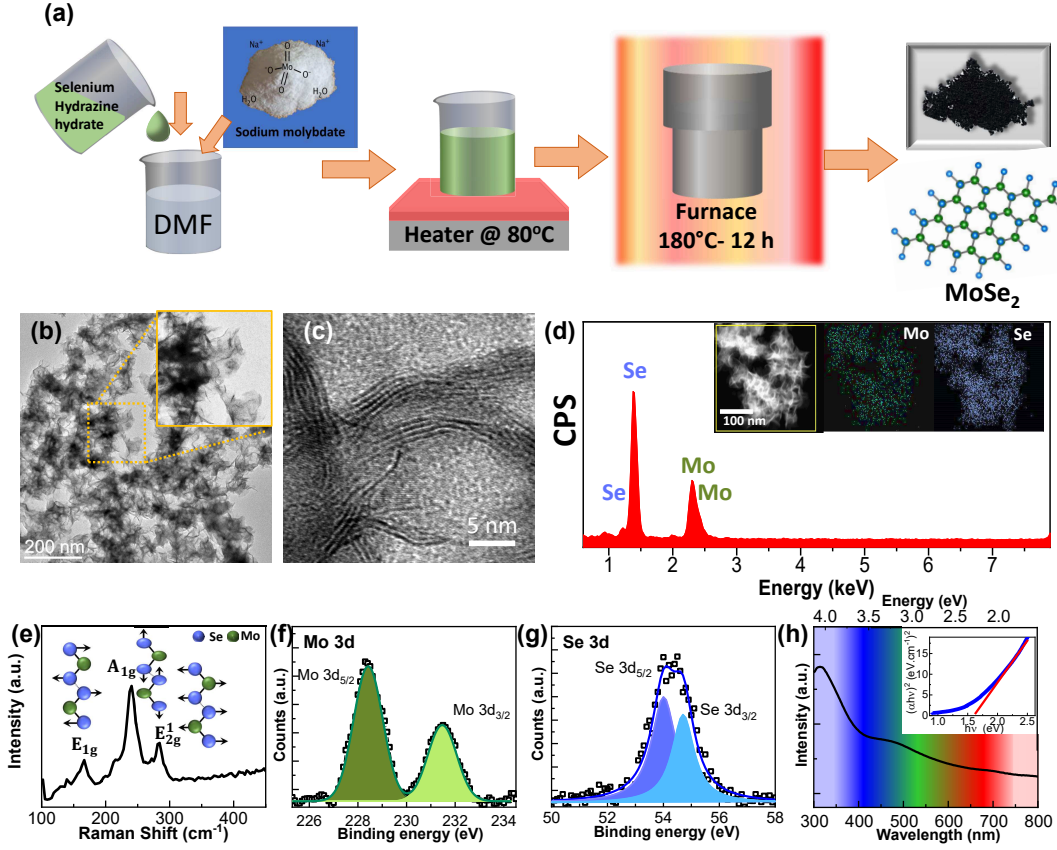


Figure 1: **Sample preparation and basic characterizations.** (a) Schematic presentation of the synthesis of MoSe₂ NFs. (b) low and high magnification (inset) TEM image of the MoSe₂ NFs. (c) HRTEM image of the individual NFs with few layer thickness. (d) EDS spectrum of the MoSe₂ NFs with their elemental mapping (inset) Mo, and Se, respectively. (e) Raman spectrum of the MoSe₂ NFs. High resolution (f) Mo 3d and (g) Se 3d binding energy spectrum of MoSe₂ NFs. (h) UV-Vis absorption spectrum of MoSe₂ NFs and its Tauc plot (inset).

to the nonlinear Kerr effect through the change in optical refractive index, n , as function intensity of the coherent Gaussian laser beam. Therefore, the propagating beam forms self-diffraction patterns in the far-field due to the spatial self-phase modulation (SSPM). The schematic representation of SSPM due to the light-matter interaction between the incident laser beam and the reoriented MoSe₂ NFs is shown in 2 (b). There are at least two different points r_1 and r_2 in the resultant outgoing Gaussian light, where the slopes of the distribution curve are same $(d\Delta\psi/dr)_{r=r_1} = (d\Delta\psi/dr)_{r=r_2}$ and they have same phase. Therefore, the output light intensity profile with the same slope points maintains constant phase differences. The diffraction ring patterns are either bright or dark as given by the following condition [14],

$$\Delta\psi(r_1) - \Delta\psi(r_2) = 2M\pi \quad (2)$$

where M is the integer number. The odd and even values of the M correspond to the dark and bright diffraction ring, respectively. Also the path difference, L_{eff} of the laser beam inside the cuvette can be determined from the following equation 3 [17, 43]

$$L_{eff} = \int_{L_1}^{L_2} \left(1 + \frac{z^2}{z_0^2}\right)^{-1} dz = z_0 \tan^{-1} \left[\frac{z}{z_0} \right]_{L_1}^{L_2}; \quad z_0 = \frac{\pi\omega_0^2}{\lambda} \quad (3)$$

where L_1 and L_2 are the distance from the focus (f) to the side of the quartz cuvette. The central intensity profile of the transmitted Gaussian beam can be expressed as $I(0, z) = 2I$, where I is the average intensity of the incident laser, z_0 is the diffraction length and w_0 is the $1/e^2$ beam radius. From the equation 1 and 3, the nonlinear refractive index (n_2) of MoSe₂ NFs can be determined as

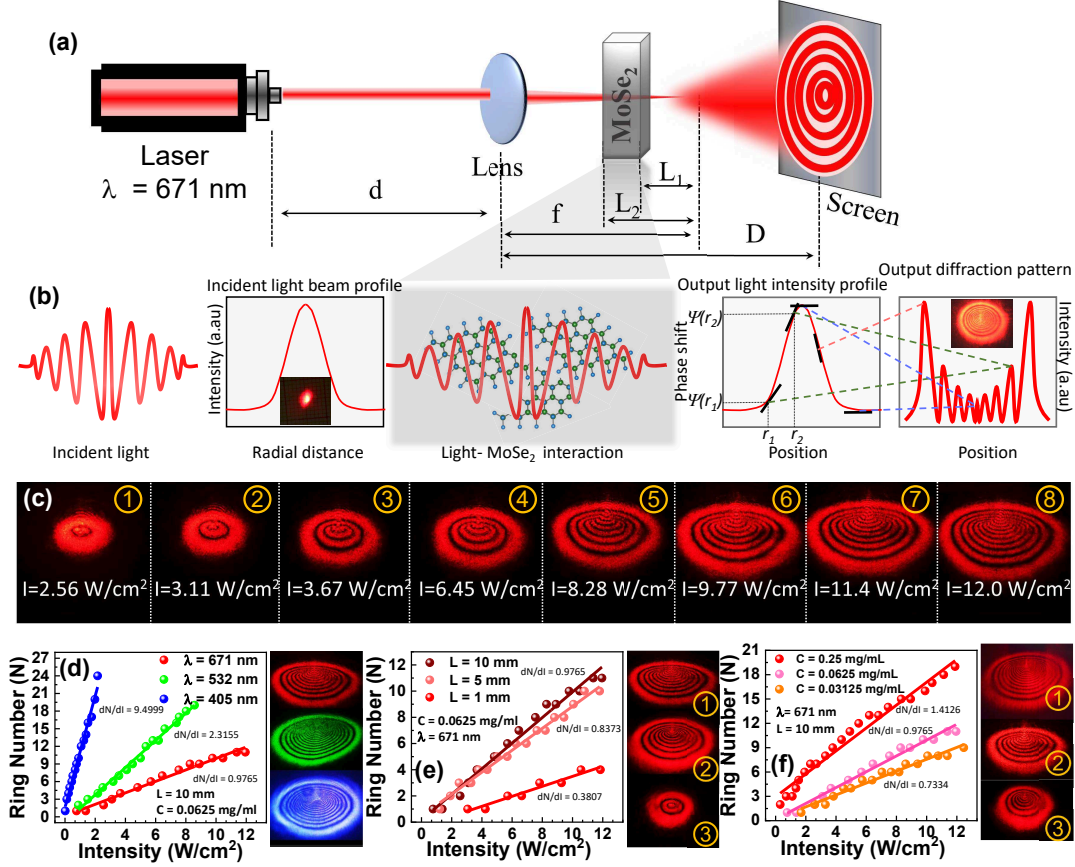


Figure 2: **Schematic of the experimental setup and SSPM in MoSe₂ NFs.** (a) Experimental setup for SSPM study of MoSe₂ NFs. (b) Schematic of the microscopic light-matter interaction process: The diffraction ring produced through the coherent interaction of light and suspended MoSe₂ NFs. (c) The evolution of diffraction ring patterns on the screen with the intensity of incident laser ($\lambda = 671$ nm). (d) The plot of diffraction ring numbers vs laser intensity for $\lambda = 405$, 532 and 671 nm. (e) The variation of diffraction ring numbers with incident laser ($\lambda = 671$ nm) intensity with cuvette lengths of 1, 5 and 10 mm. (f) The diffraction ring number vs intensity of laser ($\lambda = 671$ nm) with various concentration of MoSe₂ (0.25 mg/ml, 0.0625 mg/ml, and 0.03125 mg/ml).

$$n_2 = \frac{\lambda}{2n_0 L_{eff}} \frac{dN}{dI} \quad (4)$$

Hence, the third-order nonlinear susceptibility, ($\chi_{total}^{(3)}$), can be determined for MoSe₂ NFs using the NLO properties as [10, 19, 44]:

$$\chi_{total}^{(3)} = \frac{cn_0^2}{12\pi^2} 10^{-7} n_2 \quad (esu) \quad (5)$$

where c is the velocity of light in the free space. However, the available number of active 2D NFs of MoSe₂ present in the solvent has put a significant role on $\chi_{total}^{(3)}$, so it is necessary to determine the third-order nonlinear susceptibility for a single-layer ($\chi_{monolayer}^{(3)}$). Hence, the $\chi_{monolayer}^{(3)}$ for the single-layer MoSe₂ can be determined by [44]

$$\chi_{total}^{(3)} = \chi_{monolayer}^{(3)} \times N_{eff}^2 \quad (6)$$

where, N_{eff} represents the effective number of layers of material. This $\chi^{(3)}$ has a strong dependence on the electric field strength of the incident laser beam. The detailed calculation has been provided in the appendix section. The $\frac{dN}{dI}$ is a crucial parameter for the determination of the NLO refractive index of 2D materials.

Table 1: Nonlinear refractive index and nonlinear susceptibility estimated using SSPM spectroscopy

λ [nm]	L [mm]	C [mg/ml]	dN/dI [cm ² /W]	n_2 [cm ² /W]	$\chi_{total}^{(3)}$ [esu]	$\chi_{monolayer}^{(3)}$ [esu]
671	10	0.0625	0.975652	6.6×10^{-6}	0.00428	1.35×10^{-8}
532	10	0.0625	2.3155	1.3×10^{-5}	0.00706	2.23×10^{-8}
405	10	0.0625	9.49993	6.1×10^{-5}	0.01537	4.86×10^{-8}
671	5	0.0625	0.83735	1.1×10^{-5}	0.00735	2.32×10^{-8}
671	1	0.0625	0.38072	2.6×10^{-5}	0.01672	5.29×10^{-8}
671	10	0.25	1.41262	9.6×10^{-6}	0.0062	1.96×10^{-8}
671	10	0.03125	0.73344	4.9×10^{-6}	0.00322	1.01×10^{-8}

The Figure 2(c)(①-⑧) shows the diffraction ring patterns projected on the screen as a function of intensity of the incident light ($\lambda = 671 \text{ nm}$). With the increasing intensity of the incident light, the horizontal diameter of the rings and also the ring numbers increase linearly. The same experiment has been repeated for the other two lasers with $\lambda = 532 \text{ nm}$ and 405 nm , and the results are presented in Figure 2(d). Figure 2(d) shows the variation of the diffraction ring numbers as a function of the intensity of the laser beams. From the linear fitting of the corresponding data, the estimated slopes ($\frac{dN}{dI}$) are 0.9765, 2.3155 and 9.4999 for $\lambda = 671, 532$ and 405 nm , respectively. The results reveal that $\frac{dN}{dI}$ increases with decreasing wavelength of the laser lights. Here, the larger photon energy gives rise to higher SSPM effects consistent with other previously reported results [20, 19]. NLO responses of 2D materials are dependent not only on the photonic energy but also on a few other parameters, like available active materials and the effective length travel by the laser inside the medium. To study this effect, the concentration of MoSe₂ and the cuvette thickness have varied. Figure 2(e) shows the variation of the diffraction ring numbers as a function of laser light intensity with $\lambda=671 \text{ nm}$ for three different cuvette thicknesses. The number of diffraction rings has a dependence on the thickness of the cuvette, and their slopes are found to be 0.9765, 0.8373, and 0.3807 for cuvette length $L = 10, 5,$ and 1 mm , respectively. The corresponding diffraction ring patterns at highest intensity are presented in Figure 2(e)(①-③). Hence, the available light-matter interaction due to the presence of active materials inside the medium is also studied, as a function of laser light intensity with $\lambda=671 \text{ nm}$, by varying the concentration of MoSe₂ NFs with the fixed cuvette thickness ($L=10 \text{ mm}$). The Figure 2(f) shows the variations of diffraction rings with the incident light intensity for different concentrations, $C = 0.125, 0.0625$ and 0.03125 mg/ml and the corresponding slopes are 1.4126, 0.9760, and 0.7334, respectively. The diffraction images for the highest intensity are shown in Figure 2(f)(①-③) for $C = 0.25, 0.0625$ and 0.03125 mg/ml , respectively. From the above experiments, the n_2 and $\chi^{(3)}$ are calculated and presented in the Table 1. As evident from the results, the increment of n_2 and $\chi^{(3)}$ occurs due to an increase in the energy of the incident laser beam and the active material concentration. These results reveal that both n_2 and $\chi^{(3)}$ increase with the increasing energy of the incident laser beam. Whereas with reducing the effective travel length of the laser beam inside the medium by changing the thickness of the cuvette, n_2 and $\chi^{(3)}$ values are also increased. Similarly, with increasing the concentration of the active material, the n_2 and $\chi^{(3)}$ values are also increased.

Here, we have observed that the number of diffraction rings increases with increasing cuvette thickness and the concentration of MoSe₂ NFs. The above results can be understood from the interaction of light with the suspended NFs. The variation of $\chi^{(3)}$ and n_2 are similar in nature, as suggested from the equation 5, whereas n_2 has strong dependence on λ of incident laser, effective transmission length of the laser propagating through the medium and $\frac{dN}{dI}$ generates from the light-matter interaction. The electrons of the NFs coherently oscillate due to the strong light-matter interaction. With the increasing cuvette thickness or NFs density in the solution, effective interaction of the laser beam with materials increases. These results are observed due to the larger spatial phase shift of the laser beam leading to creates more diffraction rings.

The obtained n_2 and $\chi^{(3)}$ for MoSe₂ NFs are found to be comparatively larger than other family members of transition metal dichalcogenides (TMDs) (see Table 1 and section S2 of supplementary). The

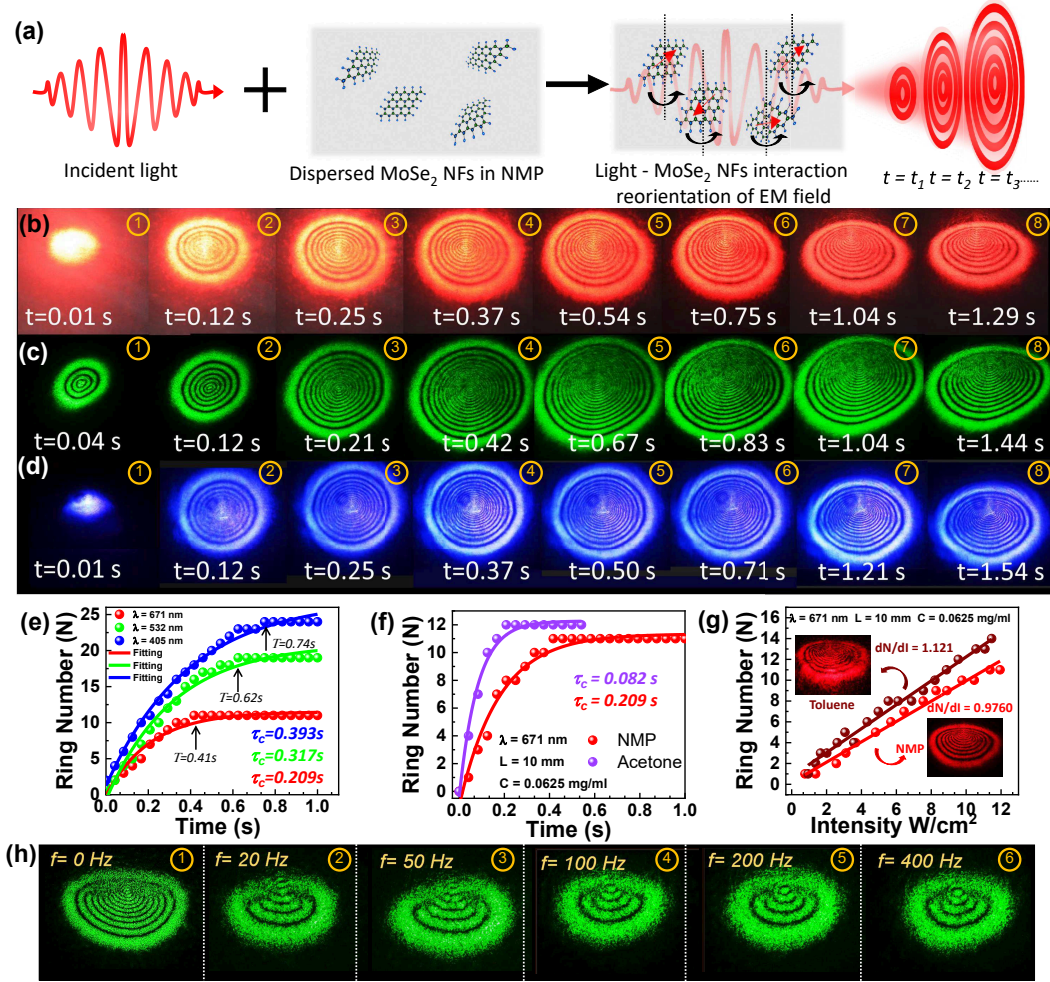


Figure 3: **The emergence of coherent light-matter interaction ('Wind-chime' model) and the thermal lens effect.** (a) Schematic presentation of the formation of SSPM patterns for MoSe₂ NFs via wind-chime model. (b-d) The diffraction ring pattern formed on the screen as function of time for $\lambda = 671, 532,$ and 405 nm, respectively. (e) The evolution of the diffraction ring numbers with time at highest intensity for $\lambda = 671, 532,$ and 405 nm. (f) The plot of diffraction ring numbers with time in different viscous medium (NMP and acetone) for $\lambda = 671$ nm. (g) The diffraction ring numbers through SSPM in both polar (NMP) and non-polar (toluene) solvent at $\lambda = 671$ nm. (h) SSPM patterns at different mechanical chopper modulation frequencies (0 - 400 Hz).

larger NLO responses compared to other TMDs can be attributed to the morphological changes and large surface area of MoSe₂[45].

2.2 SSPM: Mechanism of light-matter interaction

In the above-mentioned nonlinear Kerr effect leading to SSPM, the n_2 and $\chi^{(3)}$ are determined for the suspended MoSe₂ NFs. The self-phase modulated diffraction ring numbers increase with time to a maximum value. The time required to achieve that maximum diameter at a fixed intensity is described by the 'wind-chime' model proposed by Wu et al. [15]. According to this model, the intense laser beam polarizes (or reorients) the suspended NFs under the influence of the optical electric field through the energy relaxation process. As a result, the number of diffraction rings increases with time due to the enhanced phase modulation of the Gaussian beam from coherent interaction with the reoriented NFs. Here, the suspended NFs are considered individual domains and the reoriented NFs interact coherently with the incident laser beam. Schematic of the 'wind-chime' model has been presented in Figure 3(a). By this process, the whole system produces the SSPM through the nonlocal coherent interaction between the MoSe₂ NFs and incident laser beams.

Table 2: Diffraction ring formation time from ‘wind-chime’ model

Materials	Solvent	Wavelength λ (nm)	Intensity I (cm^2/W)	Formation time \mathcal{T} (s)	Reference
MoS ₂	NMP	532	250	0.2	[15]
MoTe ₂	NMP	750	252	0.62	[46]
Black phosphorus	NMP	700	18.9	0.7	[17]
Graphite	NMP	—	100	0.43	[8]
MoSe ₂	NMP	671	12	0.41	This
	Acetone	671	12	0.22	work

Figure 3(b-d) shows the evolution process of the SSPM of the incident light beams with different wavelengths propagating through the 2D MoSe₂ NFs. Initially, a bright spot has formed in the far-field. Gradually, a fully circular diffraction pattern emerges as the NFs become aligned along the optical field. After some time, the upper half of the diffraction rings start to collapse and slowly becomes stable. The evolution of diffraction rings over time is presented in Figure 3(b-d) for laser beams with $\lambda = 671, 532$ and 405 nm, respectively. According to the wind chime model, the time required to form the maximum diameter full circular diffraction pattern is equal to the time required to reorient these NFs along the electric field of the incident polarized light. The time evolution of the diffraction ring numbers is presented in Figure 3(e), and the dynamics of formation diffraction rings follow the exponential model as,

$$N = A (1 - e^{-t/\tau_c}) \quad (7)$$

where N is the number of rings, τ_c is the rise time for the ring formation, and A is a constant. As shown in Figure 3(e), the τ_c is estimated to be 0.209, 0.317 and 0.0393 s for 671, 532 and 405 nm, respectively. The minimum time (\mathcal{T}) required for reaching the highest number of rings is estimated to be 0.41, 0.62 and 0.74 s, respectively. According to the wind-chime model, the time required for the pattern formation is as follows [15, 17],

$$\mathcal{T} = \frac{\epsilon_r \pi \eta \xi R c}{1.72(\epsilon_r - 1) I h} \quad (8)$$

where ϵ_r is the relative dielectric constant of MoSe₂, η is the coefficient of viscosity of the solvent, R is the domain radius (~ 100 nm), h is the flake thickness (~ 5 nm), and I is the laser intensity (~ 12 W/cm²). As we know that the formation time of diffraction ring (equation no8) strongly depends on the size, thickness, and dielectric constant of the materials. Also, \mathcal{T} depends upon the viscosity (η) of the dispersion medium, and they are proportional to each other. Hence, keeping all the parameters same, if we use solvents with different viscosity, the formation time of those diffraction rings are also different. Low viscous medium requires a shorter time to reorient the 2D NFs towards incident electric field rather than high viscous medium. To verify the wind-chime model, two different viscous medium like NMP ($\eta = 1.65 \times 10^{-3}$ Pa.s) and acetone ($\eta = 3.2 \times 10^{-4}$ Pa.s) have been chosen. As expected, the theoretically estimated \mathcal{T} is found to be 0.38 and 0.26 s for NMP and acetone solvent, respectively. Also, the \mathcal{T} is estimated from the experimental data (3(f)) to be 0.41 and 0.22 s for NMP and acetone solvent, respectively. The experimental results are in good agreement with the previously reported values for other materials, as presented in table 2.

To investigate the effect of polarity of the solvent, we have used one polar (NMP) and one non-polar (toluene) solvents keeping other parameters constant. The results are presented in Figure 3(g). In both cases, similar diffraction patterns are observed, which confirms that these NLO effects are truly the properties of 2D semiconducting materials, and the nature of polarity of the solvent doesn’t play any role. In addition to the Kerr nonlinearity, the change in the temperature of the medium under an intense laser beam can also modify the refractive index of the medium and produce similar self-phase modulation as described above. The above phenomenon is known as the ‘thermal lens effect’ [47]. The SSPM is an NLO phenomenon and depends on the reorientation or polarization of the materials with an incident laser beam. In contrast, the thermal lens effect has a linear optical response [47, 48]. To confirm the origin of the diffraction rings, a mechanical chopper was introduced into the path of the incident laser beam

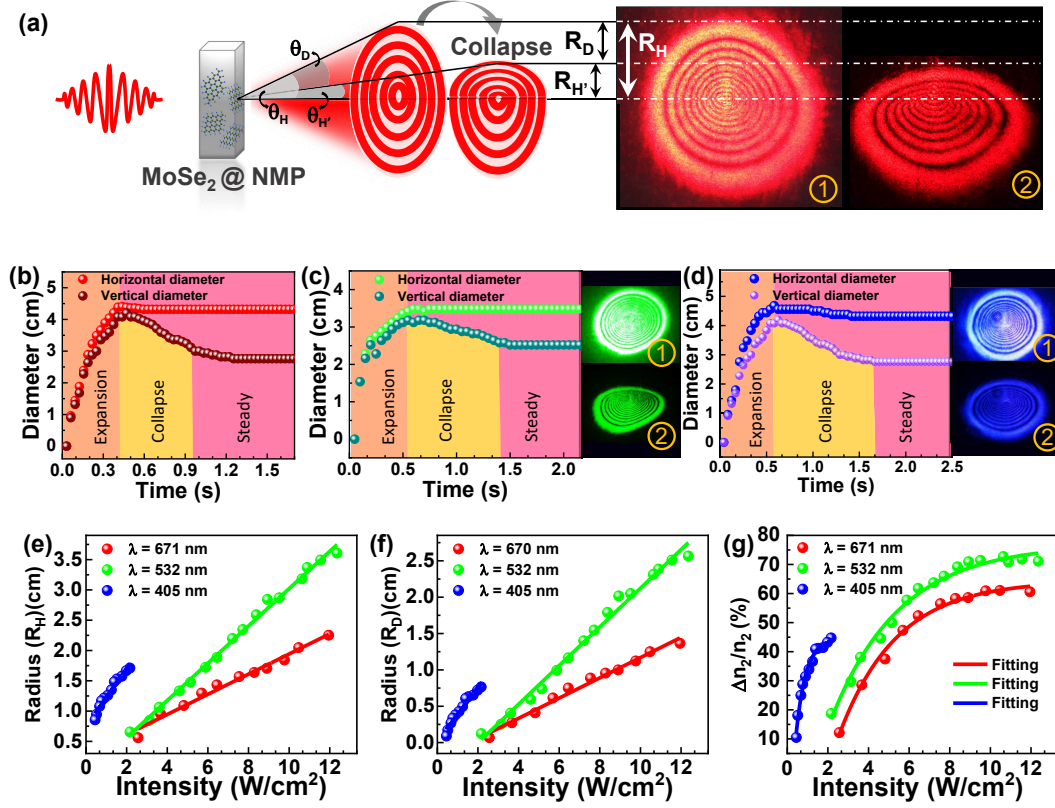


Figure 4: **Collapse phenomena of SSPM diffraction patterns.** (a) Schematic presentation of the collapse process of the diffraction ring with half-cone and distortion angle. ① and ② are the real images of the SSPM diffraction pattern at maximum and distorted condition. (b-d) The evolution of the vertical and horizontal diffraction ring diameters over time for incident laser light of $\lambda = 671, 532,$ and 405 nm, respectively. The variation in the (e) maximum radius (R_H) and (f) distorted radius (R_D) of the diffraction ring for different incident laser of $\lambda 671, 532$ and 405 nm. (g) The relative change in the nonlinear refractive index with incident light intensity for $\lambda = 671, 532,$ and 405 nm.

[27]. In our experiments, the chopper can modulate the intensity of the laser at a frequency of 20 Hz to 400 Hz [2, 20]. Figure 3(h) (①-⑥) shows the diffraction ring patterns for modulation frequency, $f = 0, 20, 50, 100, 200$ and 400 Hz, respectively. The above results show that the number of diffraction rings after using the chopper is less than those without a chopper. These observations confirm that the NLO response is the inherent feature and dominates the thermal lens effect.

2.3 Dynamics of collapse phenomena of diffraction patterns

After a close look, it has been observed that the diffraction rings are getting distorted with time. In the SSPM experiment, the diffraction ring gradually develops once the focused laser passes through MoSe₂ NFs. After the diffraction ring reaches its maxima, the upper half of the vertical radius begins to collapse towards the center. More distortion occurs along the vertical direction compared to the horizontal direction, as shown in Figure 4. To be more precise, the lower half of the diffraction rings remained stable, whereas the upper half collapses. After a few seconds, it reaches the equilibrium situation as shown in Figure 4 (a). This collapse (upper half) process is due to the non-axis-symmetrical thermal convection leading to the distortion of diffraction pattern described by Wang et al. [42]. In this process, the dispersive medium absorbs some part of the propagating laser light due to its finite optical absorption coefficient[49, 14]. As a result, the temperature gradient increases along the vertical direction around the laser spot, enhancing the thermal convection process[50]. The above convection process of the medium reduces the concentration of the 2D materials in the upper part of the medium than the lower part. Therefore, the upper part of the laser beam is less diffracted by the dispersed 2D materials leading to distorted diffraction patterns which collapse towards the center. The above phenomenon is quantified by the half-

cone angle of the diffraction pattern of the Gaussian laser beam, which can be expressed as [51]

$$\theta_H = n_2 \left[-\frac{8IrL}{w_0^2} \exp\left(-\frac{2r^2}{w_0^2}\right) \right]_{max} \quad (9)$$

where $\left[-\frac{8IrL}{w_0^2} \exp\left(-\frac{2r^2}{w_0^2}\right) \right]$ is a constant when $r \in [0, +\infty)$. As a result, θ_H is proportional to the effective nonlinear refractive index of the dispersed 2D materials.

Figure 4(a) shows the schematic presentation of the time-dependent collapse process by changing the diffraction angle. The intensity-dependent collapse behaviour of the diffraction rings can be quantified by the change of diffraction angle formed between the sample and the screen [22]. These diffraction rings are formed through a series of coaxial cones, and the distortion angles are presented as [21, 52, 53]

$$\theta_D = \theta_H - \theta_{H'} = \frac{R_H}{D} - \frac{R_{H'}}{D} = \frac{R_D}{D} \quad (10)$$

where R_H is the maximum diffraction radius, θ_H is the maximum half diffraction angle. After the distortion, the two parameters R_H and θ_H must be changed to new values of $R_{H'}$ and $\theta_{H'}$, respectively, and θ_D can also be described as a difference of nonlinear refractive index as

$$\theta_D = \theta_H - \theta_{H'} = (n_2 - n'_2)IC = \Delta n_2 IC \quad (11)$$

Therefore, the final relation between the relative change in nonlinear refractive index can be presented in terms of the ratio between the distorted and maximum half-angle as [1]

$$\frac{\Delta n_2}{n_2} = \frac{\theta_D}{\theta_H} = \frac{R_D}{R_H} \quad (12)$$

Based on the above equation 12, the distortion process of the diffraction rings is qualitatively analyzed by $\Delta n_2/n_2$ with the dynamic change of the distortion and full radius of the diffraction rings (R_D/R_H). Typically, the $\Delta n_2/n_2$ is mainly depends on the laser intensity, temperature and time [1]. Among the above three parameters (intensity, temperature, and time), the intensity of the laser beam has the most prominent dependence on the change of the nonlinear refractive index (n_2) [51, 54].

Figure 4(a)(①-②) shows the image of the diffraction ring patterns after attaining the maximum size and at the steady-state condition after the collapse process for the laser beam with $\lambda = 671$ nm. Figure 4(b-d) shows the evolution of the diffraction ring pattern over time for all three laser beams with $\lambda = 671, 532,$ and 405 nm, respectively, at their highest intense laser power. For all three lasers, the horizontal diameters increased to the maximum diameter during the expansion and remained constant for the rest of the time. At the same time, the vertical diameters reach the maximum size and then slowly collapse with time to steady-state values. Interestingly, the collapse time increases (0.54, 0.89, and 1.06 sec) with the increasing photon energy of the laser beam ($\lambda = 671, 532,$ and 405 nm). The experimentally measured maximum vertical radius (R_H) before the collapse and the radius after the collapse process (R_D) are presented in Figure 4(e-f). Here, during the collapse process, the deformation of the diffraction rings are observed due to non-axis-symmetrical thermal convection as described above.

Figure 4 (g) shows the dependence of relative change in the nonlinear refractive index with the incident laser beam intensity using the eq 12. The $\Delta n_2/n_2$ increases with increasing laser light intensity, but the relative change tends to be saturated with the increasing laser light intensity. The nonlinear effect of blue light is the strongest. The relative nonlinear refractive index $\Delta n_2/n_2$ of the MoSe₂ NFs can be found to 40% (2W/cm²), 75% (12.5W/cm²) and 60% (12W/cm²) for the incident light with $\lambda = 405, 532$ and 671 nm respectively.

2.4 Nonreciprocal light propagation in MoSe₂ based photonic diode

Here we demonstrate a novel nonlinear photonic diode device using MoSe₂/SnS₂ hybrid structure based on the SSPM. The SnS₂ is another nonlinear material that shows strong NLO response and SSPM. The

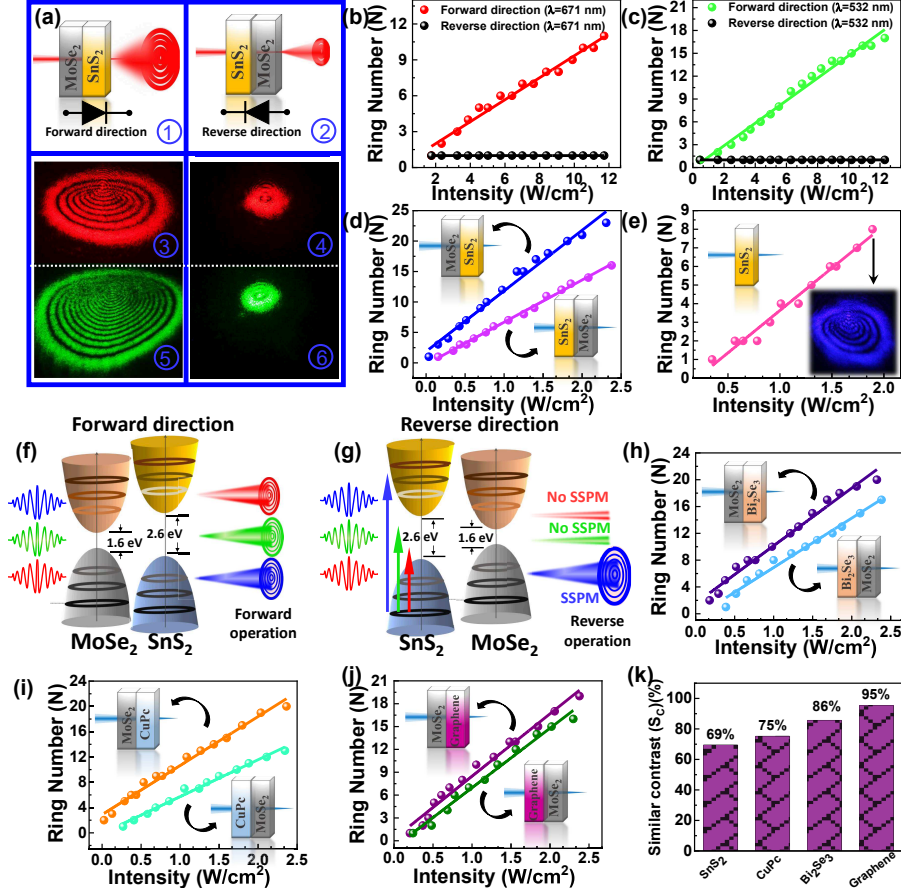


Figure 5: **Nonreciprocal light propagation in all-optical photonic diode.** (a) ① - ② shows the schematic presentation of the nonreciprocal light propagation in forward and reversed direction. ③ and ⑤ shows the diffraction patterns obtained at forward condition for $\lambda = 671$, and 532 nm, respectively. ④ and ⑥ shows the diffraction rings obtained at reversed condition for $\lambda = 671$, and 532 nm, respectively. The experimental result obtained for the nonlinear photonic diode based on MoSe₂/SnS₂ hybrid structure for incident laser light of (b) $\lambda = 671$ nm and (c) $\lambda = 532$ nm. (d) The diffraction ring numbers as a function of intensity of the incident light $\lambda = 405$ nm for the MoSe₂/SnS₂ hybrid structure. (e) The SSPM effect for independent SnS₂ dispersed in NMP excited by $\lambda = 405$ nm. (inset shows the diffraction rings at highest intensity). (f) and (g) Schematic diagram of the microscopic band diagram for all-optical forward and reverse photonic diode operation, respectively. The diffraction ring number variation for both forward and reverse direction with incident light intensity for the hybrid structure of (h) MoSe₂/Bi₂Se₃, (i) MoSe₂/CuPc (j) MoSe₂/graphene, respectively. (k) The similar contrast (S_C) of MoSe₂ comparing to other semiconducting materials (SnS₂, CuPc, Bi₂Se₃, graphene and Sb₂S₃).

SnS₂ has a bandgap (2.6 eV) larger than MoSe₂ (1.6 eV) and the hybrid structure can be used as a photonic diode for nonreciprocal light propagation[40, 19]. The laser lights with $\lambda = 532$ and 671 nm are used to characterize the photonic diode based on MoSe₂/SnS₂ hybrid structure. The photonic diode produces the diffraction pattern when the laser beams propagate in the forward direction (i.e. MoSe₂→SnS₂) as shown in Figure 5 (a) ②,④,⑥. Whereas in the reverse direction (i.e. MoSe₂←SnS₂), no such diffraction rings are observed as shown in Figure 5 (a) ①,③,⑤. In the reverse direction large absorption through SnS₂ reduces the intensity of the laser in MoSe₂. Therefore, the effect of SSPM is negligible and there is no diffraction patterns. Therefore the above properties of proposed hybrid photonic diode can be used for all-optical switch applications where the nonreciprocal propagation of light can be achieved.

Laser light intensity-dependent diffraction ring numbers with unidirectional property of MoSe₂/SnS₂ photonic diode for laser beams with $\lambda = 671$ and 532 nm, are presented in Figure 5 (b) and (c). Here the values of dN/dI are found to be 1.479 and 0.9186 for $\lambda = 532$ and 671 nm, respectively. The values are very much comparable with single MoSe₂ results. The photonic diode has a higher NLO response at $\lambda=532$ nm than $\lambda=671$ nm, and it can perform better as an optical diode at a higher wavelength.

To further check the unidirectional performance of the nonlinear photonic diode (using $\lambda = 405$ nm) in

forward and reverse operation and results are presented in Figure 5 (d). Interestingly, the diffraction rings appear in both directions, but the number of diffraction rings is different. Therefore, the MoSe₂/SnS₂ photonic diode is not appropriate for lower λ like 405 nm, and to investigate it, we have performed the SSPM for only SnS₂ using 405 nm laser and results are shown in Figure 5(e). As expected, the SSPM is observed in SnS₂ (bandgap ~ 2.6 eV) when the laser with higher excitation energy (2.71 eV) is applied [27]. To understand the basic mechanism for photonic diode application through the light-matter interaction, schematically, we present the energy band for both MoSe₂ and SnS₂ in Figure 5 (f & g) for forward and reverse, respectively.

In this experiment, three different lasers having higher energy than MoSe₂ (bandgap ~ 1.6 eV) are used, and a photon of energy $E = \hbar\omega$ can excite the electrons from the valance band to the conduction band. The excited electrons go to the ground state by releasing the photon. The emitted photons interact with the incident light and produce the diffraction rings through the optical Kerr effect [19, 27]. In this process, the excited electrons will move antiparallel with the applied optical electric field (coming from the laser beam) and polarize the suspended MoSe₂ NFs. Next, the reorientation process reduces the angle between the polarization direction and the external electric field to achieve the minimum interaction energy configuration. That increases the NLO response of 2D MoSe₂ NFs, leading to the nonlinear Kerr effect [22, 51].

However, 532 and 671 nm lasers are unable to excite the electrons in SnS₂ from valance band to conduction band and mostly get absorbed due to the intraband transitions. Therefore, no such diffraction rings are observed [19, 24, 2]. The laser beam with $\lambda = 405$ nm produces diffraction rings in both the pure SnS₂ system as well as the MoSe₂/SnS₂ photonic diode.

To further estimate the n_2 of the photonic diode MoSe₂ and few other semiconducting materials from the nonreciprocal light propagation characteristics, similar experiments were performed. The similarity comparison method (SCM) allow us to estimate similarity contrast (S_C) of these materials using their nonlinear refractive indices as [19],

$$\begin{aligned} S_C = 1 - D_C &= 1 - \frac{|n_{21} - n_{12}|}{n_{21}} \\ &= 1 - \frac{\left| \frac{\lambda}{2n_0 L_{eff}} \frac{dN_1}{dI_1} - \frac{\lambda}{2n_0 L_{eff}} \frac{dN_2}{dI_2} \right|}{\frac{\lambda}{2n_0 L_{eff}} \frac{dN_1}{dI_1}} \\ &= 1 - \frac{\left| \frac{N_1}{I_1} - \frac{N_2}{I_2} \right|}{\frac{N_1}{I_1}} \end{aligned} \quad (13)$$

where D_C is the difference constant, n_{21} and n_{22} represent the nonlinear refractive index of the hybrid system obtained for the forward and reverse direction respectively. The semiconducting Bi₂Se₃, CuPc, and graphene are used in combination with MoSe₂ for S_C studies which has been presented in Figure 5(h-j) and summary of the results is presented in Figure 5(k). The S_C values for SnS₂, CuPc, Bi₂Se₃ and graphene are found to be 69%, 75%, 86% and 95%, respectively. This results indicate that the MoSe₂ has similar nonlinear refractive index to the graphene [19, 8, 55, 42]. Furthermore, the CuPc has very low S_C which is close to SnS₂ for $\lambda = 405$ nm.

2.5 Cross-phase modulation: MoSe₂ - based all-optical switching and logic gates

By taking advantage of the SSPM by MoSe₂ NFs, an all-optical switch has been demonstrated to perform the logical function like an OR gate as shown in Figure 6. The schematic of the experimental logical OR gate is presented in Figure 6 (a) using the cross-phase modulation (XPM) technique [56, 44]. Two lasers with different wavelengths are used as the two input signals ("A" and "B") of the logic system on the MoSe₂ NFs based logic device. The resultant XPM are the corresponding outputs of the logic gate. Figure 6(b) shows the symbol and switch circuit of the OR logic gate. Where the input "A" or "B" is in high-level "1", the output "Y" will also be in high-level "1", and only when both are at the lower level "0", the output will be low "0". The corresponding switching waveforms are ("A", "B", and

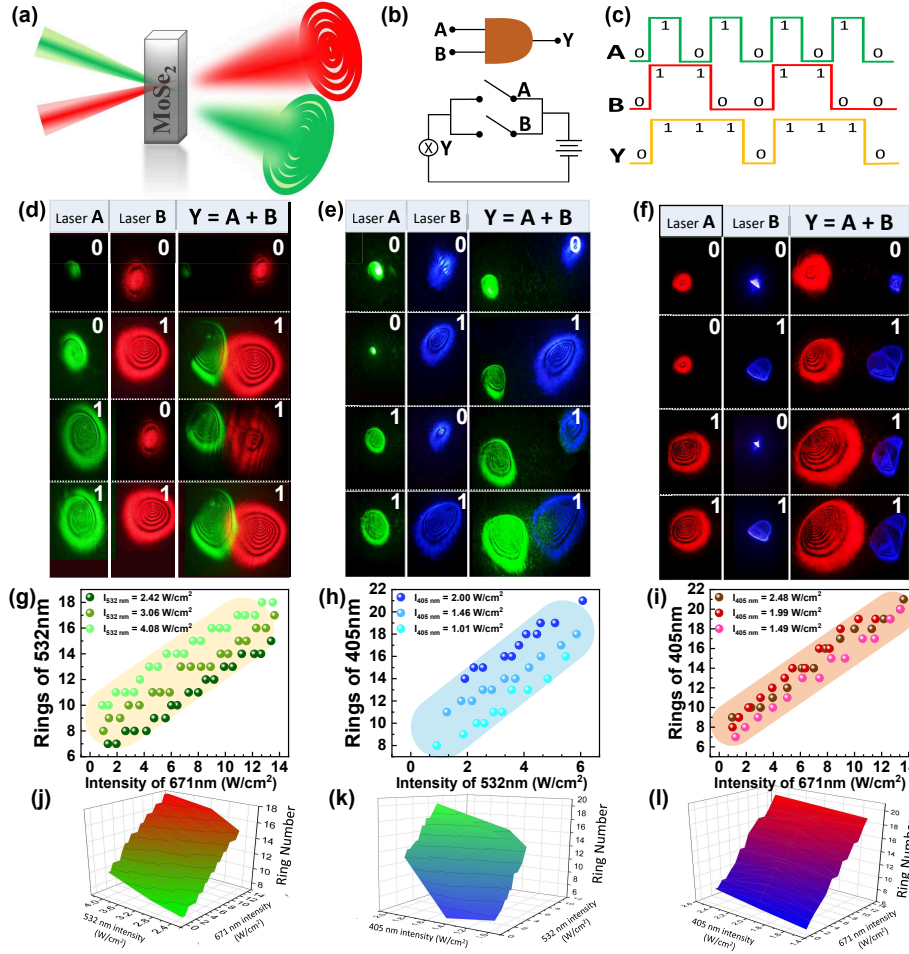


Figure 6: **Cross-phase modulation: All-optical switching and logic gates.** (a) Schematic presentation of the XPM inside MoSe₂ NFs for photonic diode application. (b) Symbol and circuit model of the logical OR gate. (c) The waveform of OR gate (input: *A* and *B*; output: *Y*) (d-f) MoSe₂ based experimental results for optical OR gate operation using two-color XPM technique for the combination of $\lambda = 532$ & 671 nm, 405 & 532 nm, and 405 & 671 nm, respectively. (g-i) Change in the diffraction ring numbers of the probe lasers vs the intensity variation of the pump laser. (j-l) Three dimensional presentation of the two-color XPM for different pair of lasers ($\lambda = 532$ & 671 nm, 405 & 532 nm, and 405 & 671 nm).

”*Y*”) presented in Figure 6 (c). Here, all the logic levels are realized by the number of diffraction rings formed using the XPM process. Here, we observed a two-laser-based system to achieve light-light modulation. The diffraction rings cannot be formed when the incident light or probe light is too low to interact with the sample, and in this case, only a Gaussian light appears on the screen. When another laser light (pump light) with relatively high intensity is cross-modulated with the Gaussian probe light, it can form diffraction rings on the screen for both the lights. The individual lights of $\lambda = 532$ nm and 671 nm are considered input ”*A*” and input ”*B*”, respectively. Now both lights are cross-coupled, and the final image is formed on the screen, which is considered as the output ”*Y*”. Based on the output using two-lasers, we can build an optical logic OR gate, which is presented in Figure 6 (d-f) for the combination of laser lights with $\lambda = 532$ & 671 nm, 405 & 532 nm, and 405 & 671 nm, respectively. Figure 6(g) presents the number of diffraction rings of the probe light ($\lambda = 532$ nm) with the intensity signal of the pump light $\lambda = 671$ nm, where the probe light intensities are 2.42 , 3.06 and 4.08 W/cm^2 , respectively. The initial number of diffraction rings formed by the probe light depends on the intensity of the probe light. The diffraction rings are modulated based on the superposition principle when the pump light is on. In addition, the diffraction ring numbers of the probe light linearly depend on the pump light’s intensity. For other two set of light combinations, $\lambda = 405$ & 532 nm, and 405 & 671 nm, the similar experiments are performed and presented in Figure 6 (g) and (i), respectively. Figure 6 (j-l) shows the three dimensional

model of the overall data obtained through the diffraction ring numbers of the probe light with the intensity of the pump and probe light for choice of pump and probe lights with $\lambda = 532$ & 671 nm, 405 & 532 nm, and 405 & 671 nm, respectively.

3 Conclusions

In conclusion, we have reported the spatial self-phase modulation (SSPM) of Gaussian laser beams by suspended MoSe₂ nanoflakes (NFs) in a solvent. The NFs of 2D layered MoSe₂ are synthesized using a cost-effective solvothermal technique. The nonlinear broadband optical response of MoSe₂ NFs has been investigated using laser beams with $\lambda = 671, 532,$ and 405 nm. The nonlinear refractive index and the monolayer third-order nonlinear susceptibility are estimated from the change in the diffraction ring number as a function of laser power. The obtained n_2 and $\chi_{(monolayer)}^{(3)}$ for MoSe₂ NFs are found to be 1.3×10^{-5} cm²/W and 2.23×10^{-8} esu, respectively at 532 nm excitation laser, are comparatively larger than other family members of TMDs. The large values of n_2 and $\chi^{(3)}$ reveal strong nonlinear coherent interaction of light with the ensemble of layered 2D MoSe₂ NFs. The evolution (formation) of the self diffraction ring patterns due to SSPM have been described by the ‘wind-chime’ model considering coherent light-matter interactions. Based on the SSPM, a passive photonic diode has been designed using MoSe₂/SnS₂ hybrid heterostructures to demonstrate the nonreciprocal light propagation. The unidirectional properties of the above photonic diode using MoSe₂ have been compared with a few other semiconducting materials (i.e., Bi₂Se₃, CuPc, and graphene) by the similarity comparison method. The all-optical switching properties have also been explored based on the two-color interband coherence. In addition, the all-optical information processing has been examined by performing the ‘‘OR’’ logic gate operation using cross-phase modulation (XPM) of two laser beams. We believe that these NLO phenomena can provide an inroad foundation for the MoSe₂ based all-optical switching as optical diodes and logic devices.

4 Experimental Section

Synthesis of MoSe₂ nanoflakes:

Facile solvothermal technique has been adapted to synthesize MoSe₂ nanoflakes (NFs), and Figure 1 (a) shows the schematic presentation of the synthesis process. The detailed preparation method of MoSe₂ NFs has been discussed in our earlier works [28, 57]. In brief, a suitable amount of sodium molybdate ($Na_2MoO_4 \cdot 2H_2O$) was added in 22.5 ml dimethylformamide (DMF) solution with 30 min sonication for proper dispersion at room temperature. Next, 15 mg of selenium powder is dispersed in 7.5 ml hydrazine hydrate by constant stirring in an oil bath at 80°C for 1h. Then, this solution was mixed with the previously prepared DMF solution to maintain the atomic ratio of Mo: Se is 1:2. Then, the as-prepared solution was transferred into a 100 ml autoclave up to 60 % of its volume and kept into an oven, which was already preheated at 180°C for the next 12 h. Thereafter, the autoclave was cooled down by natural cooling. Next, the obtained precipitate was filtered and washed by de-ionized water and ethanol multiple times. Finally, the black MoSe₂ powder was annealed at 450°C under N₂ atmosphere for 4 h to improve the crystallinity of MoSe₂ NFs.

Synthesis of SnS₂ nanosheets:

The synthesis process of SnS₂ has been done following process reported by Zhang *et al.*[58]. Typically, 220 mg $SnCl_4 \cdot 5H_2O$ and 280 mg thioacetamide were mixed with 60 mL of de-ionized water and then transferred to a 100 mL Teflon-lined autoclave and the autoclave was heated and kept at 180°C for 24 hours. After the reaction, the autoclave was allowed to cool naturally to room temperature, and the yellow-colored sample was collected after centrifuging the sample at 10000 rpm. The final product was dried in a hot air oven at 80°C for 6 hours and stored in a desiccator. The detailed characterization has been carried out and discussed in the section S1 of supplementary.

Characterization:

Field-emission scanning electron microscope (FESEM Hitachi S-4800) and transmission electron microscopy (FEG-TEM) were used to characterize the sample morphology. Figure 1 (b) and (c) shows the layered MoSe₂ NFs. TEM-EDX (transmission electron microscopy-energy-dispersive X-ray spectroscopy) spectrum and elemental mapping reveals the chemical composition and stoichiometric ratios of MoSe₂ NFs (see Figure 1(d)). The above analysis confirms that the sample contains the elements Mo and Se with their atomic ratio is about 1: 2.07. Figure 1 (e) shows the Raman spectrum of 2D MoSe₂ NFs with its characteristics in-plane (E_{1g} , E_{2g}^1) and out-of-plane (A_{1g}) vibrational modes. The high-resolution X-ray photoelectron spectroscopy (XPS) shows the chemical environment of an element Mo 3d and Se 3d, which are presented in Figure 1 (f) and (g), respectively. The bandgap of the MoSe₂ NFs sample was determined to be $E_g = 1.6$ eV by the UV-Vis absorption curve and corresponding Tauc plot curve as shown in Figure 1 (h). The characterized 2D layered MoSe₂ NFs have been dispersed in NMP (N-methyl-2-pyrrolidone) and a few other solvents (acetone, toluene, etc.) with different loading concentrations for the SSPM experiments.

Experimental setup:

The schematic of SSPM spectroscopy setup to study the NLO response of MoSe₂ NFs suspended in NMP solvent is shown in Figure 2(a). The sample shows the broadband SSPM effect for the incident pump light with $\lambda = 671, 532,$ and 405 nm, respectively. Here, the pump laser passes through the convex lens of 20 cm focal length (f) and incident on a quartz cuvette of the thickness of 10 mm, which is placed near the focal point of the lens. Under intense coherent Gaussian laser beam, the suspended MoSe₂ NFs interact with the incident laser and the MoSe₂ NFs start to orient along the optical electric field [59].

Supporting Information

Supporting Information is available from the Wiley Online Library or from the author.

Acknowledgements

This work is supported by the ‘Department of Science and Technology’ under startup research grant (Grant No. SRG/2019/000674). One of the authors, K. K. Chattopadhyay acknowledges the University Grants Commission, Govt. of India, under the ‘University with potential for excellence II’ (UPE II) scheme. The author, MS gratefully acknowledges DST ‘INSPIRE’ scheme [IF170868] for giving research opportunities through fellowship. AB & SB thanks CSIR Govt. of India for Research Fellowship with Grant No. 09/080(1109)/2019-EMR-I & 09/080(1110)/2019-EMR-I, respectively. The authors want to thank Dr Sudipta Bera for his valuable support in preliminary discussions and setting-up the experiment. His contribution is very much appreciated for this project.

Conflict of Interest

The authors declare no competing financial interest.

References

- [1] Yunlong Liao, Chunmei Song, Yuanjiang Xiang, and Xiaoyu Dai. Recent advances in spatial self-phase modulation with 2d materials and its applications. *Annalen der Physik*, 532(12):2000322, 2020.
- [2] Leiming Wu, Xixi Yuan, Dingtao Ma, Ye Zhang, Weichun Huang, Yanqi Ge, Yufeng Song, Yuanjiang Xiang, Jianqing Li, and Han Zhang. Recent advances of spatial self-phase modulation in 2d materials and passive photonic device applications. *Small*, 16(35):2002252, 2020.
- [3] Xue-jun Zhang, Zhen-hua Yuan, Rui-xin Yang, Yi-lin He, Ying-lin Qin, Si Xiao, and Jun He. A review on spatial self-phase modulation of two-dimensional materials. *Journal of Central South University*, 26(9):2295–2306, 2019.
- [4] J.W. You, S.R. Bongu, Q. Bao, and N.C. Panoiu. Nonlinear optical properties and applications of 2d materials: theoretical and experimental aspects. *Nanophotonics*, 8(1):63–97, 2019.

- [5] Teng Tan, Xiantao Jiang, Cong Wang, Baicheng Yao, and Han Zhang. 2d material optoelectronics for information functional device applications: Status and challenges. *Advanced Science*, 7(11):2000058, 2020.
- [6] Sergei K. Turitsyn, Anastasia E. Bednyakova, Mikhail P. Fedoruk, Serguei B. Papernyi, and Wallace R. L. Clements. Inverse four-wave mixing and self-parametric amplification in optical fibre. *Nature Photonics*, 9(9):608–614, 2015.
- [7] Chang Wang, Si Xiao, Xingcheng Xiao, Haixia Zhu, Li Zhou, Yiduo Wang, Xiaojing Du, Yingwei Wang, Zhongjian Yang, Ran Duan, Mianzeng Zhong, Horst-Günter Rubahn, Gufei Zhang, Yejun Li, and Jun He. Nonlinear optical response of sbi nanorods dominated with direct band gaps. *J. Phys. Chem. C*, 125(28):15441–15447, July 2021.
- [8] Y. L. Wu, L. L. Zhu, Q. Wu, F. Sun, J. K. Wei, Y. C. Tian, W. L. Wang, X. D. Bai, Xu Zuo, and Jimin Zhao. Electronic origin of spatial self-phase modulation: Evidenced by comparing graphite with c60 and graphene. *Applied Physics Letters*, 108(24):241110, 2016.
- [9] Yuen-Ron Shen. Principles of nonlinear optics. 1984.
- [10] Robert W. Boyd. *Nonlinear optics*. Academic press, 2020.
- [11] Yue Jia, Yunlong Liao, Leiming Wu, Youxian Shan, Xiaoyu Dai, Houzhi Cai, Yuanjiang Xiang, and Dianyuan Fan. Nonlinear optical response, all optical switching, and all optical information conversion in nbse2 nanosheets based on spatial self-phase modulation. *Nanoscale*, 11:4515–4522, 2019.
- [12] S. D. Durbin, S. M. Arakelian, and Y. R. Shen. Optical-field-induced birefringence and fredericksz transition in a nematic liquid crystal. *Phys. Rev. Lett.*, 47:1411–1414, Nov 1981.
- [13] S. D. Durbin, S. M. Arakelian, and Y. R. Shen. Strong optical diffraction in a nematic liquid crystal with high nonlinearity. *Opt. Lett.*, 7(4):145–147, Apr 1982.
- [14] Rui Wu, Yingli Zhang, Shichao Yan, Fei Bian, Wenlong Wang, Xuedong Bai, Xinghua Lu, Jimin Zhao, and Enge Wang. Purely coherent nonlinear optical response in solution dispersions of graphene sheets. *Nano Lett.*, 11(12):5159–5164, December 2011.
- [15] Yanling Wu, Qiong Wu, Fei Sun, Cai Cheng, Sheng Meng, and Jimin Zhao. Emergence of electron coherence and two-color all-optical switching in mos2 based on spatial self-phase modulation. *Proceedings of the National Academy of Sciences*, 2015.
- [16] Si Xiao, Ying Ma, Yilin He, Yiduo Wang, Hao Xin, Qi Fan, Jingdi Zhang, Xiaohong Li, Yu Zhang, Jun He, and Yingwei Wang. Revealing the intrinsic nonlinear optical response of a single mos2 nanosheet in a suspension based on spatial self-phase modulation. *Photon. Res.*, 8(11):1725–1733, Nov 2020.
- [17] Jingdi Zhang, Xuefeng Yu, Weijia Han, Bosai Lv, Xiaohong Li, Si Xiao, Yongli Gao, and Jun He. Broadband spatial self-phase modulation of black phosphorous. *Opt. Lett.*, 41(8):1704–1707, Apr 2016.
- [18] Yilin He, Jingdi Zhang, Si Xiao, Yingwei Wang, and Jun He. Effect of concentration on the formation time of diffraction rings in spatial self-phase modulation. *Chin. Opt. Lett.*, 20(1):011901, Jan 2022.
- [19] Leiming Wu, Yuze Dong, Jinlai Zhao, Dingtao Ma, Weichun Huang, Ye Zhang, Yunzheng Wang, Xiantao Jiang, Yuanjiang Xiang, Jianqing Li, Yaqing Feng, Jialiang Xu, and Han Zhang. Kerr nonlinearity in 2d graphdiyne for passive photonic diodes. *Advanced Materials*, 31(14):1807981, 2019.
- [20] Youxian Shan, Zhongfu Li, Banxian Ruan, Jiaqi Zhu, Yuanjiang Xiang, and Xiaoyu Dai. Two-dimensional bi2s3-based all-optical photonic devices with strong nonlinearity due to spatial self-phase modulation. *Nanophotonics*, 8(12):2225–2234, 2019.

- [21] Yue Jia, Youxian Shan, Leiming Wu, Xiaoyu Dai, Dianyuan Fan, and Yuanjiang Xiang. Broadband nonlinear optical resonance and all-optical switching of liquid phase exfoliated tungsten diselenide. *Photon. Res.*, 6(11):1040–1047, Nov 2018.
- [22] Jie Li, Zilong Zhang, Jun Yi, Lili Miao, Jing Huang, Jinrui Zhang, Yuan He, Bin Huang, Chujun Zhao, Yanhong Zou, and Shuangchun Wen. Broadband spatial self-phase modulation and ultrafast response of mxene $\text{ti}_3\text{c}_2\text{tx}$ ($t=\text{o, oh or f}$). *Nanophotonics*, 9(8):2415–2424, 2020.
- [23] Lili Miao, Bingxin Shi, Jun Yi, Yaqin Jiang, Chujun Zhao, and Shuangchun Wen. Ultrafast nonlinear optical response in solution dispersions of black phosphorus. *Scientific Reports*, 7(1):3352, 2017.
- [24] Leiming Wu, Ye Zhang, Xixi Yuan, Feng Zhang, Weichun Huang, Dingtao Ma, Jinlai Zhao, Yunzheng Wang, Yanqi Ge, Hao Huang, Ning Xu, Jianlong Kang, Yuanjiang Xiang, Yupeng Zhang, Jianqing Li, and Han Zhang. 1d@0d hybrid dimensional heterojunction-based photonics logical gate and isolator. *Applied Materials Today*, 19:100589, 2020.
- [25] Xiaohong Li, Kunhong Hu, Bosai Lyu, Jingdi Zhang, Yingwei Wang, Peng Wang, Si Xiao, Yongli Gao, and Jun He. Enhanced nonlinear optical response of rectangular mos_2 and $\text{mos}_2/\text{tio}_2$ in dispersion and film. *J. Phys. Chem. C*, 120(32):18243–18248, August 2016.
- [26] Amir Reza Sadrolhosseini, Suraya Abdul Rashid, Hamid Shojanazeri, A. S. M. Noor, and Hossein Nezakati. Spatial self-phase modulation patterns in graphene oxide and graphene oxide with silver and gold nanoparticles. *Optical and Quantum Electronics*, 48(4):222, 2016.
- [27] Yunlong Liao, Qian Ma, Youxian Shan, Junwu Liang, Xiaoyu Dai, and Yuanjiang Xiang. All-optical applications for passive photonic devices of tas_2 nanosheets with strong kerr nonlinearity. *Journal of Alloys and Compounds*, 806:999–1007, 2019.
- [28] Supratim Maity, Biswajit Das, Madhupriya Samanta, Bikram Kumar Das, Shrabani Ghosh, and Kalyan Kumar Chattopadhyay. Mose_2 -amorphous cnt hierarchical hybrid core-shell structure for efficient hydrogen evolution reaction. *ACS Appl. Energy Mater.*, 3(5):5067–5076, May 2020.
- [29] Hua Tang, Hong Huang, Xiaoshuai Wang, Kongqiang Wu, Guogang Tang, and Changsheng Li. Hydrothermal synthesis of 3d hierarchical flower-like mose_2 microspheres and their adsorption performances for methyl orange. *Applied Surface Science*, 379:296–303, 2016.
- [30] M. Kristl and M. Drogenik. Synthesis of nanocrystalline mose_2 by sonochemical reaction of se with $\text{mo}(\text{co})_6$. *Inorganic Chemistry Communications*, 6(1):68–70, 2003.
- [31] J. Etzkorn, H. A. Therese, F. Rucker, N. Zink, U. Kolb, and W. Tremel. Metal–organic chemical vapor deposition synthesis of hollow inorganic-fullerene-type mos_2 and mose_2 nanoparticles. *Advanced Materials*, 17(19):2372–2375, 2005.
- [32] Jing Yang, Chunde Wang, Huanxin Ju, Yuan Sun, Shiqi Xing, Junfa Zhu, and Qing Yang. Integrated quasiplane heteronanostructures of $\text{mose}_2/\text{bi}_2\text{se}_3$ hexagonal nanosheets: Synergetic electrocatalytic water splitting and enhanced supercapacitor performance. *Advanced Functional Materials*, 27(48):1703864, 2017.
- [33] Shun Mao, Zhenhai Wen, Suqin Ci, Xiaoru Guo, Kostya (Ken) Ostrikov, and Junhong Chen. Perpendicularly oriented $\text{mose}_2/\text{graphene}$ nanosheets as advanced electrocatalysts for hydrogen evolution. *Small*, 11(4):414–419, 2015.
- [34] Feier Niu, Jing Yang, Nana Wang, Dapeng Zhang, Weiliu Fan, Jian Yang, and Yitai Qian. Mose_2 -covered n,p-doped carbon nanosheets as a long-life and high-rate anode material for sodium-ion batteries. *Advanced Functional Materials*, 27(23):1700522, 2017.
- [35] G. Kline, K. Kam, D. Canfield, and B.A. Parkinson. Efficient and stable photoelectrochemical cells constructed with wse_2 and mose_2 photoanodes. *Solar Energy Materials*, 4(3):301–308, 1981.

- [36] Jianjun Li, Yi Zhang, Wei Zhao, Dahyun Nam, Hyeonsik Cheong, Li Wu, Zhiqiang Zhou, and Yun Sun. A temporary barrier effect of the alloy layer during selenization: Tailoring the thickness of mose2 for efficient cu2znsnse4 solar cells. *Advanced Energy Materials*, 5(9):1402178, 2015.
- [37] Pratik M. Pataniya, Sanjay A. Bhakhar, Mohit Tannarana, Chetan Zankat, Vikas Patel, G.K. Solanki, K.D. Patel, Prafulla K. Jha, Dattatray J. Late, and C.K. Sumesh. Highly sensitive and flexible pressure sensor based on two-dimensional mose2 nanosheets for online wrist pulse monitoring. *Journal of Colloid and Interface Science*, 584:495–504, 2021.
- [38] Wenhui Wang, Yanling Wu, Qiong Wu, Jiaojiao Hua, and Jimin Zhao. Coherent nonlinear optical response spatial self-phase modulation in mose2 nano-sheets. *Scientific Reports*, 6(1):22072, 2016.
- [39] Bingxin Shi, Lili Miao, Qingkai Wang, Juan Du, Pinghua Tang, Jun Liu, Chujun Zhao, and Shuangchun Wen. Broadband ultrafast spatial self-phase modulation for topological insulator bi2te3 dispersions. *Applied Physics Letters*, 107(15):151101, 2015.
- [40] Chunmei Song, Yunlong Liao, Yuanjiang Xiang, and Xiaoyu Dai. Liquid phase exfoliated boron nanosheets for all-optical modulation and logic gates. *Science Bulletin*, 65(12):1030–1038, 2020.
- [41] Yunlong Liao, Youxian Shan, Leiming Wu, Yuanjiang Xiang, and Xiaoyu Dai. Liquid-exfoliated few-layer inse nanosheets for broadband nonlinear all-optical applications. *Advanced Optical Materials*, 8(9):1901862, 2020.
- [42] Gaozhong Wang, Saifeng Zhang, Fadhil A. Umran, Xin Cheng, Ningning Dong, Darragh Coghlan, Ya Cheng, Long Zhang, Werner J. Blau, and Jun Wang. Tunable effective nonlinear refractive index of graphene dispersions during the distortion of spatial self-phase modulation. *Applied Physics Letters*, 104(14):141909, 2014.
- [43] Si Xiao, Yi-lin He, Yu-lan Dong, Yi-duo Wang, Li Zhou, Xue-jun Zhang, Ying-wei Wang, and Jun He. Near-infrared spatial self-phase modulation in ultrathin niobium carbide nanosheets. *Frontiers in Physics*, 9:212, 2021.
- [44] Youxian Shan, Leiming Wu, Yunlong Liao, Jie Tang, Xiaoyu Dai, and Yuanjiang Xiang. A promising nonlinear optical material and its applications for all-optical switching and information converters based on the spatial self-phase modulation (sspm) effect of tase2 nanosheets. *J. Mater. Chem. C*, 7:3811–3816, 2019.
- [45] Gangshuo Liu, Shuxi Dai, Peng Li, Baohua Zhu, Zhenkun Wu, and Yuzong Gu. Preparation and comparison of nonlinear optical properties of mose2 with different types of structures. *Optical Materials*, 95:109240, 2019.
- [46] Lili Hu, F. Sun, H. Zhao, and Jimin Zhao. Nonlinear optical response spatial self-phase modulation in mote2: correlations between $\chi^{(3)}$ and mobility or effective mass. *Opt. Lett.*, 44(21):5214–5217, Nov 2019.
- [47] F. W. Dabby, T. K. Gustafson, J. R. Whinnery, Y. Kohanzadeh, and P. L. Kelley. Thermally self-induced phase modulation of laser beams. *Applied Physics Letters*, 16(9):362–365, 1970.
- [48] Yanan Wang, Yingjie Tang, Peihong Cheng, Xufeng Zhou, Zhuan Zhu, Zhaoping Liu, Dong Liu, Zhiming Wang, and Jiming Bao. Distinguishing thermal lens effect from electronic third-order nonlinear self-phase modulation in liquid suspensions of 2d nanomaterials. *Nanoscale*, 9:3547–3554, 2017.
- [49] Jun Wang, Yenny Hernandez, Mustafa Lotya, Jonathan N. Coleman, and Werner J. Blau. Broadband nonlinear optical response of graphene dispersions. *Advanced Materials*, 21(23):2430–2435, 2009.

- [50] Chao Teng, Liying Su, Jingxin Chen, and Jianfeng Wang. Flexible, thermally conductive layered composite films from massively exfoliated boron nitride nanosheets. *Composites Part A: Applied Science and Manufacturing*, 124:105498, 2019.
- [51] Gaozhong Wang, Saifeng Zhang, Xiaoyan Zhang, Long Zhang, Ya Cheng, Daniel Fox, Hongzhou Zhang, Jonathan N. Coleman, Werner J. Blau, and Jun Wang. Tunable nonlinear refractive index of two-dimensional mos₂, ws₂, and mose₂ nanosheet dispersions (invited). *Photon. Res.*, 3(2):A51–A55, Apr 2015.
- [52] Leiming Wu, Zhongjian Xie, Lu Lu, Jinlai Zhao, Yunzheng Wang, Xiantao Jiang, Yanqi Ge, Feng Zhang, Shunbin Lu, Zhinan Guo, Jie Liu, Yuanjiang Xiang, Shixiang Xu, Jianqing Li, Dianyuan Fan, and Han Zhang. Few-layer tin sulfide: A promising black-phosphorus-analogue 2d material with exceptionally large nonlinear optical response, high stability, and applications in all-optical switching and wavelength conversion. *Advanced Optical Materials*, 6(2):1700985, 2018.
- [53] M.D. Zidan, M.S. EL-Daher, M.M. Al-Ktaifani, A. Allahham, and A. Ghanem. Spatial phase modulation and all-optical switching of tris(2',2-bipyridyl)iron(ii) tetrafluoroborate. *Optik*, 219:165275, 2020.
- [54] Yue Jia, Zhongfu Li, Muhammad Saeed, Jie Tang, Houzhi Cai, and Yuanjiang Xiang. Kerr nonlinearity in germanium selenide nanoflakes measured by z-scan and spatial self-phase modulation techniques and its applications in all-optical information conversion. *Opt. Express*, 27(15):20857–20873, Jul 2019.
- [55] Youxian Shan, Jie Tang, Leiming Wu, Shunbin Lu, Xiaoyu Dai, and Yuanjiang Xiang. Spatial self-phase modulation and all-optical switching of graphene oxide dispersions. *Journal of Alloys and Compounds*, 771:900–904, 2019.
- [56] Lu Lu, Wenhui Wang, Leiming Wu, Xiantao Jiang, Yuanjiang Xiang, Jianqing Li, Dianyuan Fan, and Han Zhang. All-optical switching of two continuous waves in few layer bismuthene based on spatial cross-phase modulation. *ACS Photonics*, 4(11):2852–2861, November 2017.
- [57] Biswajit Das, Arnab Bera, Madhupriya Samanta, Satyabrata Bera, Sk Kalimuddin, Mohan Kundu, Sirshendu Gayen, Kalyan Kumar Chattopadhyay, and Mintu Mondal. Resistive switching in a mose₂-based memory device investigated using conductance noise spectroscopy. *ACS Appl. Electron. Mater.*, 3(7):3096–3105, July 2021.
- [58] Jun Zhang, Guozhou Huang, Jinghui Zeng, Yuxuan Shi, Songjun Lin, Xuan Chen, Hongbo Wang, Zhe Kong, Junhua Xi, and Zhenguo Ji. High carriers transmission efficiency zns/sns₂ heterojunction channel toward excellent photoelectrochemical activity. *Journal of the American Ceramic Society*, 102(5):2810–2819, 2019.
- [59] Si Xiao, Yu Zhang, Ying Ma, Yiduo Wang, Yilin He, Jingdi Zhang, Yongqiang Jiang, Xiaohong Li, Ruixin Yang, Jun He, and Yingwei Wang. Observation of spatial self-phase modulation induced via two competing mechanisms. *Opt. Lett.*, 45(10):2850–2853, May 2020.
- [60] D. J. Clark, V. Senthilkumar, C. T. Le, D. L. Weerawarne, B. Shim, J. I. Jang, J. H. Shim, J. Cho, Y. Sim, M.-J. Seong, S. H. Rhim, A. J. Freeman, K.-H. Chung, and Y. S. Kim. Erratum: Strong optical nonlinearity of cvd-grown mos₂ monolayer as probed by wavelength-dependent second-harmonic generation [phys. rev. b 90, 121409(r) (2014)]. *Phys. Rev. B*, 92:159901, Oct 2015.
- [61] Heming Xia, Xinyu Chen, Song Luo, Feng Qin, Alexander Idelevich, Saptarshi Ghosh, Toshiya Ideue, Yoshihiro Iwasa, Alla Zak, Reshef Tenne, Zhanghai Chen, Wei-Tao Liu, and Shiwei Wu. Probing the chiral domains and excitonic states in individual ws₂ tubes by second-harmonic generation. *Nano Lett.*, 21(12):4937–4943, June 2021.

Supporting Information: Nonlinear coherent light-matter interaction in 2D MoSe₂ nanoflakes for all-optical switching and logic applications

• Laser induced SSPM in optically nonlinear materials

2D materials are drawing much more attention in the field of nonlinear optical (NLO) which can be quantitatively described using basic Electrodynamics and theories of light-matter interactions. Generally, the NLO effect occurs when an intense laser beam modulates the optical properties of the material. The optical responses of the materials are reacted in a nonlinear manner with the power of the incident laser beam. To visualize this effect mathematically, the applied electric field ($\tilde{E}(t)$) can be expressed by expanding the resulting polarization ($\tilde{P}(t)$), has both the linear and the nonlinear contributions, given by equation 14:

$$\begin{aligned}\tilde{P}(t) &= \tilde{P}_L(t) + \tilde{P}_{NL}(t) \\ &= \tilde{P}_L^{(1)}(t) + \tilde{P}^{(2)}(t) + \tilde{P}^{(3)}(t) + \dots \\ &= \epsilon_0 [\chi^{(1)}\tilde{E}(t) + \chi^{(2)}\tilde{E}^2(t) + \chi^{(3)}\tilde{E}^3(t) + \dots]\end{aligned}\quad (14)$$

where ϵ_0 is the vacuum permittivity and the coefficients $\chi^{(n)}$ are the n^{th} -order susceptibilities of the materials. The first coefficient $\chi^{(1)}$ is the linear susceptibility and also it is a tensor of rank two. $\chi^{(1)}$ describes the linear optical responses, such as absorption and refraction of the materials. The quantities $\chi^{(2)}$ and $\chi^{(3)}$ are known as the second- and third-order NLO susceptibilities, respectively, which are normally much weaker than $\chi^{(1)}$. When the optical field is strong enough, the phenomena caused by higher-order ($n \geq 2$) terms become significant, which could induce new radiation at different frequencies, pulse shaping, or change of refractive index [10]. The emergence of nonlinear optics has been the focus of modern research after the breakthrough discovery of the second-harmonic-generation (SHG) in the strong-optical-field regime. Numerous phenomena in condensed matter systems is probed in past decades using SHG technique [60, 61].

The third-order NLO susceptibility $\chi^{(3)}$ can also give rise to different NLO effects, such as third-harmonic-generation (THG), four-wave mixing (FWM), optical Kerr effect (leading to self-phase modulation), and saturable absorption (SA). Although higher-order NLO interactions are much weaker than second- and third-order NLO, and appears at extremely high laser intensity [9].

Theory of self-phase modulation and spectral broadening

NLO phenomena can be quantitatively described using Electrodynamics and theories of light-matter interaction. For self-phase modulation and spectral broadening when the propagation of a laser beam in an isotropic medium can be described by the wave equation of a plane wave:

$$\begin{aligned}\left[\nabla^2 - \frac{n_0^2}{c^2} \frac{\partial^2}{\partial t^2}\right] \tilde{E}(t) &= \frac{1}{\epsilon_0 c^2} \frac{\partial^2 \tilde{P}_{NL}(t)}{\partial t^2} \\ \text{where, } \tilde{E}(t) &= \tilde{E}_0(\omega) [e^{+i\omega t} + e^{-i\omega t}] \\ \text{and, } \tilde{P}_{NL}^{(3)} &= \epsilon_0 \chi^{(3)} \tilde{E}_0^3(\omega) [e^{+i\omega t} + e^{-i\omega t}]^3\end{aligned}\quad (15)$$

where $\tilde{E}(t)$ is the optical field, n_0 is the linear refractive index, and c is the speed of light in a vacuum. $\tilde{P}_{NL}^{(3)}$ of a material gives rise to optical phenomena like THG and intensity dependent refractive index. Time domain nonlinear polarization function ($\tilde{P}_{NL}^{(3)}(t)$) is shown as Eqn(16)

$$\tilde{P}_{NL}^{(3)}(r, t) = \epsilon_0 \int_{-\infty}^{+\infty} \int_{-\infty}^{+\infty} \int_{-\infty}^{+\infty} R^3((z - t_1), (t - t_2), (t - t_3)) \tilde{E}(\vec{r}, t_1) \tilde{E}(\vec{r}, t_2) \tilde{E}(\vec{r}, t_3) dt_1 dt_2 dt_3 \quad (16)$$

Therefore, the effective susceptibility (χ_{eff}) can be derive from the equation 14 and 15 as ,

$$\chi_{eff} = \chi^{(1)} + 3\chi^{(3)}|\tilde{E}(\omega)|^2 \quad (17)$$

Also from the Kerr nonlinear optical relation, we may write $n = n_0 + \bar{n} + \langle \tilde{E}^2 \rangle$. Here, \bar{n}_2 is a new optical constant (the rate at which the refractive index increases with increasing optical intensity) than nonlinear refractive index (n_2). If we put the values \tilde{E} from equation 15 in above expression, we can get $\langle \tilde{E}^2 \rangle = 2\tilde{E}(\omega)\tilde{E}(\omega)^* = 2|\tilde{E}(\omega)|^2$. Hence, the refractive index of materials can be expressed as,

$$n = n_0 + 2\bar{n}_2|\tilde{E}(\omega)|^2 \quad (18)$$

In order to relate the nonlinear susceptibility $\chi^{(3)}$ to the nonlinear refractive index n_2 , from the equation 17 and 18, we can write it as,

$$\begin{aligned} n^2 &= 1 + \chi_{eff} \\ \left[n_0 + 2\bar{n}_2|\tilde{E}(\omega)|^2 \right]^2 &= 1 + \chi^{(1)} + 3\chi^{(3)}|\tilde{E}(\omega)|^2 \end{aligned} \quad (19)$$

Expanding the term up to the order of $|\tilde{E}(\omega)|^2$, the above expression can be expanded as, $n_0^2 + 4n_0\bar{n}_2|\tilde{E}(\omega)|^2 = (1 + \chi^{(1)}) + [3\chi^{(3)}|\tilde{E}(\omega)|^2]$, which shows that the linear and nonlinear refractive indices are related to the linear and nonlinear susceptibilities by

$$\begin{aligned} n_0 &= (1 + \chi^{(1)})^{1/2} \\ &\& \\ \bar{n}_2 &= \frac{3\chi^{(3)}}{4n_0} \end{aligned} \quad (20)$$

Also as we know the time-averaged intensity of the optical field which can be given by $I = 2n_0\epsilon_0c|\tilde{E}(\omega)|^2$, where, from the Kerr equation we can get $2\bar{n}_2|\tilde{E}(\omega)|^2 = n_2I$. By solving the above expressions, we can get the relation between n_2 and \bar{n}_2 as follow:

$$n_2 = \frac{\bar{n}_2}{n_0\epsilon_0c} \quad (21)$$

Solving the \bar{n}_2 , we can get $\chi^{(3)}$ as,

$$\chi^3 = \frac{4n_0^2\epsilon_0c}{3}n_2 \quad (22)$$

The above equation in SI and Gaussian unit can be express as,[9, 10]

$$\begin{aligned} n_2 \left(\frac{m^2}{W} \right) &= \frac{283}{n_0^2} \chi^{(3)} \left(\frac{m^2}{V^2} \right) \quad (SI) \\ n_2 \left(\frac{cm^2}{W} \right) &= \frac{12\pi^2}{n_0^2c} 10^7 \chi^{(3)} \left(\frac{m^2}{V^2} \right) \quad (esu) \end{aligned} \quad (23)$$

This figure "VCH-logo.png" is available in "png" format from:

<http://arxiv.org/ps/2206.12564v1>

This figure "bio-placeholder.jpg" is available in "jpg" format from:

<http://arxiv.org/ps/2206.12564v1>

This figure "placeholder-image.png" is available in "png" format from:

<http://arxiv.org/ps/2206.12564v1>